Nanoscale

PAPER

View Article Online
View Journal | View Issue

Cite this: *Nanoscale*, 2023, **15**, 13049

Multifunctional metal selenide-based materials synthesized *via* a one-pot solvothermal approach for electrochemical energy storage and conversion applications†

Bhimanaboina Ramulu, Shaik Junied Arbaz, Manchi Nagaraju and Jae Su Yu *

Highly-efficient electroactive materials with distinctive electrochemical features, along with suitable strategies to prepare hetero-nanoarchitectures incorporating two or more transition metal selenides, are currently required to increase charge storage ability. Herein, a one-pot solvothermal approach is used to develop iron–nickel selenide spring-lawn-like architectures (FeNiSe SLAs) on nickel (Ni) foam. The porous Ni foam scaffold not only enables the uniform growth of FeNiSe SLAs but also serves as an Ni source. The effect of reaction time on their morphological and electrochemical properties is investigated. The FeNiSe-15 h electrode shows high areal capacity (493.2 μA h cm^{-2}) and superior cycling constancy. The as-assembled aqueous hybrid cell (AHC) demonstrates high areal capacity and a decent rate capability of 59.4% (50 mA cm^{-2}). The AHC exhibits good energy and power densities, along with excellent cycling stability. Furthermore, to confirm its practicability, the AHC is employed to drive portable electronic appliances by charging it with wind energy. The electrocatalytic activity of FeNiSe-based materials to complete the oxygen evolution reaction (OER) is explored. Among them, the FeNiSe-15 h catalyst shows good OER performance at a current density of 50 mA cm^{-2}. This general synthesis approach may initiate a strategy of advanced metal selenide-based materials for multifunctional applications.

Received 6th May 2023,
Accepted 17th July 2023

DOI: 10.1039/d3nr02103c

rsc.li/nanoscale

1. Introduction

Recently, supercapacitors (SCs), which are renewable energy power sources with the greatest potential, have attracted a lot of attention from the scientific community because of their quick rechargeability, high power density, and increased cycling stability. It is undeniably necessary to investigate more effective electrodes to achieve the required energy density while compromising on power density and cycling stability.[1–5] As a result, several research initiatives are ongoing with the goal of establishing asymmetric/hybrid SC assemblies utilizing suitable electrodes.[6–8] Precise electrode material engineering may greatly boost the visual electrochemical properties of SCs.

Together with advances in energy storage systems, the production of hydrogen (H_2) *via* water-splitting approach has also gained a huge following as it acts as an alternative to fossil fuels.[9,10] Nevertheless, to produce H_2 gas, one of the half reactions, oxygen evolution reaction (OER), includes a four-electron transfer, which is a slow reaction that needs additional overpotential values.[11,12] A reliable catalyst substance is, consequently, important to separate water with rapid electrokinetics and low overpotentials as well. Unfortunately, although noble metal (Ru, Ir, Pt, *etc.*)-based oxides/hydroxides have revealed their superiority in the splitting of water, their extensive practicability has been inadequate to an excessive degree, mainly owing to their high cost and insufficiency of resources. Thus, other catalysts have emerged designed to exclude noble metals without sacrificing rapid transfer, durability, or low cost.[13–15]

Compared to metal oxides/hydroxides, transition metal selenide (TMSe) materials have been classified as a new family of electrodes with intensely modified capacitive capabilities, owing to their improved redox-active sites, inherently improved faradaic reactions, strong electrical conductivity, natural abundance, and definitive electrocatalytic activity.[16–20] In particular, iron selenide type of electrodes are promising active materials for energy storage systems because of their high electrochemical features and low cost.[21–24] Nevertheless, their wide

Department of Electronics and Information Convergence Engineering, Institute for Wearable Convergence Electronics, Kyung Hee University, 1732 Deogyeong-daero, Giheung-gu, Yongin-si, Gyeonggi-do 17104, Republic of Korea.
E-mail: jsyu@khu.ac.kr

†Electronic supplementary information (ESI) available: Materials, chemicals, characterizations, formulae, electrochemical measurements, and an aqueous hybrid cell that is energy harvested by a wind turbine. Also, the electrochemical performances of FeNiSe-12 h, FeNiSe-18 h, and AC electrodes are included. See DOI: https://doi.org/10.1039/d3nr02103c

application is still hampered by their lack of structural stability and synergetic properties. One approach to addressing these issues is to create binary/multi-component transition metals. Selecting suitable materials for the fabrication of an electrode material can enhance electrochemical reactions and conductivity. Some metals, such as nickel (Ni), are able to achieve desirable conductivity.[25] Additionally, the grouping of various transition metals in the arrangement of binary and ternary metals can afford good electrical conductivity. Dual iron–nickel selenide (FeNiSe) materials are considered an adaptable path for combining new functions, such as electrochemical performance and electronic arrangement, in synergetic combination as active materials for SCs/OER/HER with improved redox reactions, easy assembly, and environmental friendliness.[26–31] Furthermore, to attain a higher energy density without sacrificing power density or cycling stability, structural characteristics must be fine-tuned by constructing nanostructures with more easily available active portions, large surface area, and porous morphologies.[32]

The determination of the active center in FeNiSe is an area of ongoing research and scientific debate.[33] The composition of FeNiSe suggests that both Fe and Ni play significant roles in catalytic activity. Previous studies have suggested different hypotheses regarding the active site. According to the Sabatier principle and studies on metal hydr(oxy)oxides,[34] it has been proposed that Ni might be the active site due to its optimal interaction strength with OH_{ad}. This hypothesis suggests that Ni facilitates the OER process by providing an optimal surface for the adsorption and reaction of oxygen species.[35] On the other hand, the presence of Fe in FeNiSe is believed to influence the charge contribution and enhance the OER performance. The absorption of Fe impurities has been reported to activate partial charge transfer, improving the conductivity of Ni-based electrocatalysts. Furthermore, Lee *et al.* reported on NiFe layered double hydroxides (LDHs), demonstrating that Fe sites dominate the catalysis and exhibit significantly higher activity than Ni sites.[36] A different perspective proposed by Chen *et al.* suggested that Fe^{4+} species are not directly responsible for the OER activity.[37] However, the theoretical results indicate that high-spin Fe^{4+} facilitates the formation of an active oxygen radical intermediate. They proposed that Ni^{4+} species catalyze the subsequent O–O coupling and that the synergistic interaction between Fe and Ni is responsible for the optimal OER performance. These diverse findings indicate that the electronic structures of Ni and Fe in FeNiSe are integral to the mechanism driving enhanced OER activity. Further understanding of and control over these electronic structures is crucial for unlocking the underlying pathways involved.[38]

Conventional electroactive materials are often synthesized by a slurry coating approach in the presence of passive components (*i.e.*, super P, polyvinylidene fluoride, *etc.*) that certainly result in increased inner resistance and poor ion availability to the porous design, thus leading to low electrochemical performance.[39–42] Therefore, the direct design of TMSe on conductive three-dimensional (3D) frameworks successfully avoids the typical electrode fabrication method and eliminates the "dead-mass" surface of the active electrode. Furthermore, the binder-free strategy of preparing the electrode by *in situ* procedures increases electrical conductivity by generating flexible electron-directing pathways between active materials and supporting current collectors, increasing the surface area of the electroactive material, and emphasizing the penetration of electrolyte ions, which results in superior energy storage features with advantageous rates.[43,44]

Considering the above discussion, we proposed a new approach for designing FeNiSe spring-lawn-like architectures (SLAs) as binder-free electroactive materials by a one-pot solvothermal method without further selenization process. The FeNiSe SLAs were prepared at various reaction times under constant temperature to investigate their morphological properties and electrochemical reactions. The growth of FeNiSe architectures provides an adequate volume for versatile intercalation/de-intercalation of incoming ions due to the synergistic effect with many open pores between the vertically developed building blocks, resulting in rapid electrochemical activities and subsequently boosting charge storage capacity. Interestingly, during the growth process, Ni foam serves as both the Ni source and conductive current collector. The battery-type electroactive materials have interesting morphological and compositional benefits, including dual metal combination, a large number of active portions, and visible surfaces as well as robust electrical interaction with the underlying current collector. Moreover, the optimized FeNiSe electrode was used as a positive electrode to assemble an aqueous hybrid cell (AHC) by employing activated carbon (AC)-coated Ni foam as a negative electrode. Also, the fabricated AHC devices were demonstrated to power up portable electronics.

2. Experimental procedure

The ESI† section contains detailed information about chemicals, materials, material characterizations, and electrochemical tests.

The binder-free FeNiSe SLAs were prepared *via* the *in situ* solvothermal technique without other selenization processes. Before the growth of FeNiSe SLAs, to ensure well-cleaned surfaces, the Ni foam substrate was first cleaned with HCl solution, acetone, and deionized (DI) water under ultrasonic treatment and dried under nitrogen flow, followed by drying in a vacuum oven. Briefly, 100 mM of $NaBH_4$, 40 mM of Se powder, and 20 mM of $FeCl_3{\cdot}6H_2O$ were dissolved in 20 mL of DI water and 60 mL of ethylene glycol under constant stirring for 45 min. Then, the mixed solution was transferred to a Teflon-lined autoclave, and the Ni foam was positioned vertically in it. After that, the solvothermal-assisted reaction was carried out at 160 °C for 15 h. The resultant FeNiSe SLAs loaded on the Ni foam were collected by washing with water and ethanol at least three times to remove partially attached particles and finally desiccated in a vacuum oven overnight. The weight of the loaded active material on Ni foam was estimated by deducting the mass of bare Ni foam from the weight of

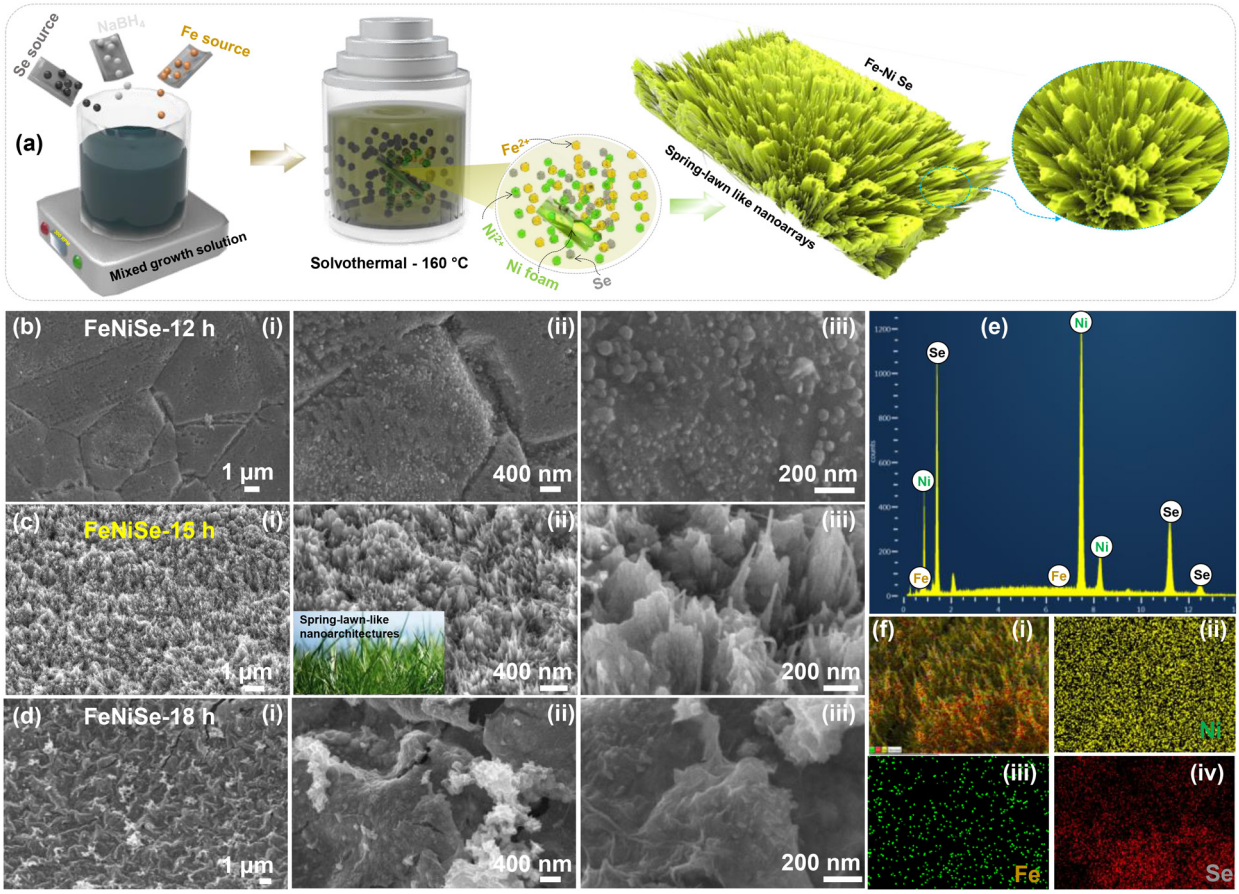

Fig. 1 (a) Schematic diagram illustrating the preparation of the FeNiSe SLAs. Low- and high-magnification FE-SEM images of the (b) FeNiSe-12 h, (c) FeNiSe-15 h, and (d) FeNiSe-18 h materials. (e) EDX spectrum and (f) elemental mapping images of the FeNiSe-15 h material.

FeNiSe-loaded Ni foam, and it was estimated to be 4.33 mg cm^{-2}. Moreover, to explore the effect of reaction time on the morphology and electrochemical performance, 12 h (2.58 mg cm^{-2}) and 18 h (3.85 mg cm^{-2}) were also used at the same temperature.

3. Results and discussion

The design and construction of FeNiSe SLAs are presented in Fig. 1(a). A simple and cost-effective straightforward solvothermal method at 160 °C was chosen to design the FeNiSe heterostructures on the conductive Ni foam substrate with robust internal construction. Fe^{2+} ions were released from their respective sources during the solvothermal process. Meanwhile, Ni^{2+} ions were liberated from the Ni foam to act as a self-sacrificial template.[45,46] Se powder and $NaBH_4$ were used as Se sources and reducing agents, respectively. The underlying porous Ni foam as the conductive substrate with low electrical resistance and large specific surface area could hasten electron transportation by enabling the shortest pathways in electrochemical activity, while the developed active material provides higher electrochemical properties. Generally, the fabrication method of binary FeNiSe through an *in situ* selenization process contains two or three key stages: *i.e.*, nucleation, growth, and coarsening. Se powder was initially reduced to produce Se^{2-} ions, which then interacted with Fe^{2+} and Ni^{2+} ions to nucleate the FeNiSe compound.

A field-emission scanning electron microscope (FE-SEM) was employed to study the surface structures of the synthesized materials. Fig. 1(b–d) depicts the surface morphological features of the FeNiSe SLAs obtained at various growth times of 12, 15, and 18 h (FeNiSe-12 h, FeNiSe-15 h, and FeNiSe-18 h), respectively. From Fig. 1(b-(i)), it is clear that the surface of Ni foam became slightly rougher after 12 h of response time compared to the original surface. The magnified FE-SEM images (Fig. 1(b-(ii) and (iii))) confirm that the surface of Ni foam was a little rough with small nanoparticle shapes. The SLAs might be starting to be formed, suggesting that the reaction time of 12 h might not be sufficient for perfect growth. The FeNiSe-12 h material usually provides poor electroactive sites. At the increased reaction time of 15 h, the low-magnification FE-SEM image in Fig. 1(c) reveals the homogeneous formation of FeNiSe SLAs on the Ni foam. From Fig. 1 (c-(ii)), FeNiSe had a vertically grown spring-lawn-like nanoarchitectured morphology. Furthermore, the high-magni-

fication FE-SEM image of Fig. 1(c-(iii)) seems to show more gaps, which could be more beneficial for the electrolyte reservoirs. The achieved nanoarchitectures may represent several oxidation and reduction processes by supplying a large number of electroactive sites. Additionally, the nano-sized spaces between them are more conducive to efficient electrolyte ion transport when evaluating electrochemical properties. Besides, when the reaction time was further extended to 18 h, the SLAs completely disappeared, as presented in Fig. 1(d-(i–iii)), leading to a decreased number of active sites and slow electrolyte transport. Also, the overwhelming assembly of SLAs may not cling rigidly to the Ni foam substrate. The existence of the Fe, Ni, and Se elements in the prepared FeNiSe-15 h material was investigated by energy-dispersive X-ray (EDX) analysis (Fig. 1(e)). The layered electronic image and elemental mapping images (Fig. 1(f-(i–iv))) also confirmed the uniform formation of the Fe, Ni, and Se elements in the synthesized FeNiSe-15 h sample.

Transmission electron microscope (TEM) analysis was further employed to explore the detailed morphological features of the prepared material. Fig. 2(a) shows the TEM image of the FeNiSe-15 h material, which is well matched with the FE-SEM images. In addition, the high-resolution (HR) TEM image (Fig. 2(b)) was further measured, which consists of two different sets of lattice fringes. One lattice fringe with a *d*-spacing value of ~2.7 Å corresponds to the (101) plane in $Ni_{0.85}Se$. The other lattice fringe with a *d*-spacing value of ~2.8 Å is related to the (004) plane in Fe_3Se_4. The mixed phase of the prepared material was further confirmed by TEM analysis. The selected area electron diffraction (SAED) pattern of the FeNiSe-15 h material was measured, as presented in Fig. 2(c). Bright rings can be observed in the SAED pattern, signifying the polycrystalline nature of the FeNiSe-15 h sample. Moreover, the X-ray diffraction (XRD) pattern of the designed FeNiSe-12 h is depicted in Fig. 2(d). Clearly, three strong peaks located at 2 theta values of 44.1°, 51.5°, and 76.1° are attributed to the diffraction patterns of Ni foam. The low-intensity peaks of the FeNiSe-15 h material could be attributed to the standard monoclinic phase of Fe_3Se_4 (JCPDS card No#01-073-2021) and hexagonal $Ni_{0.85}Se$ (JCPDS card No#00-018-0888).

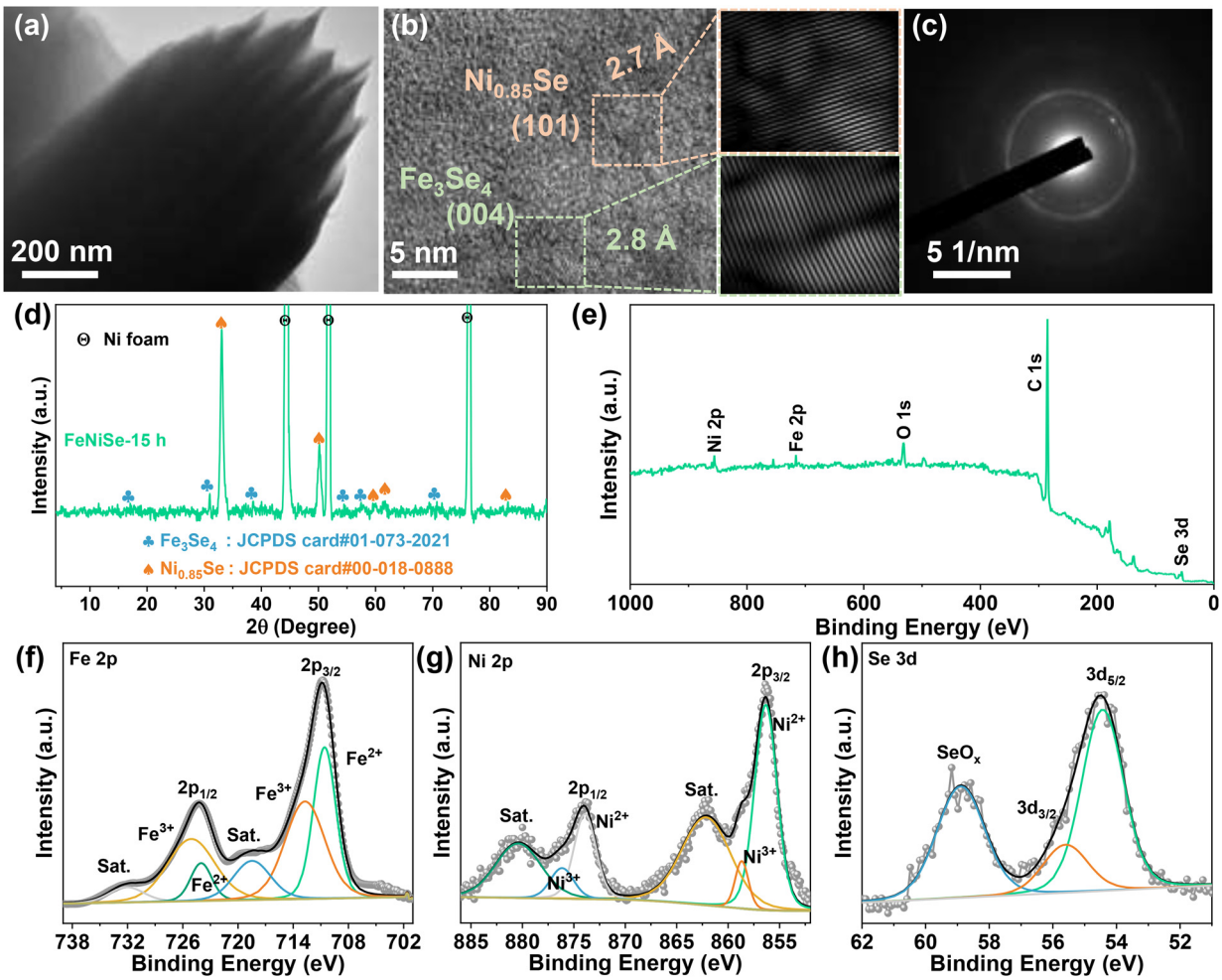

Fig. 2 (a) TEM image, (b) HR-TEM images, and (c) SAED pattern of the prepared FeNiSe-15 h material. (d) XRD pattern and (e) XPS survey scan spectrum of the prepared FeNiSe-15 h material. (f–h) Core-level spectra of Fe 2p, Ni 2p, and Se 3d, respectively.

The obtained results suggest that the FeNiSe heterostructures appear as mixed phases. Furthermore, an X-ray photoelectron spectroscopy (XPS) study was performed to obtain information on component oxidation states and chemical compositions in the prepared material. Fig. 2(e) shows the XPS survey scan spectrum, further confirming the existence of Fe, Ni, and Se elements in the FeNiSe-15 h material. In addition, due to surface exposure, carbon (C 1s) and oxygen (O 1s) elements occurred, as identified in the XPS survey scan spectrum. Fig. 2(f) displays the Fe 2p high-resolution spectrum that contains two main peaks owing to the spin–orbit doublets (Fe $2p_{3/2}$ and Fe $2p_{1/2}$ at 711.1 and 725.8 eV, respectively). Moreover, both peaks can be split into two peaks at the binding energies of 710.5, 724, 713.5, and 725.5 eV, which confirms the presence of Fe^{2+} and Fe^{3+}. Additionally, two satellite peaks could be found at 718.4 and 732.1 eV.[47] Likewise, the Ni 2p spectrum (Fig. 2(g)) contains two pairs of spin–orbit splittings arising at $2p_{3/2}$ and $2p_{1/2}$ along with two satellite peaks. The peaks at the binding energies of around 856.3 and 873 eV are related to Ni^{2+}, while the peaks at 858.6 and 876.1 eV correspond to Ni^{3+}.[48] Fig. 2(h) shows the core-level spectrum of Se 3d. From this figure, the binding energy values are identified as 54.4 and 55.6 eV, which are correlated with the Se species binding with metals in the prepared material. Moreover, the peak at 58.8 eV corresponds to Se–O bonding, which reveals the surface oxidation of Se element.[49,50] These results suggest that FeNiSe heterostructures favor increased electrochemical reactions and show tolerance for ion transportation.

Electrochemical measurements with a traditional three-electrode cell configuration in 2 M KOH electrolyte were performed to explore the advantages of the fabricated FeNiSe heterostructures for charge storage devices. Fig. 3(a) shows the comparative cyclic voltammetry (CV) curves of the prepared electrodes measured within the given potentials from 0 to 0.6 V *vs.* Ag/AgCl at a constant sweep rate of 10 mV s^{-1}. The fabricated electrodes (FeNiSe-12 h, FeNiSe-15 h, and FeNiSe-18 h) exhibited a couple of redox peaks that coincide with reversible

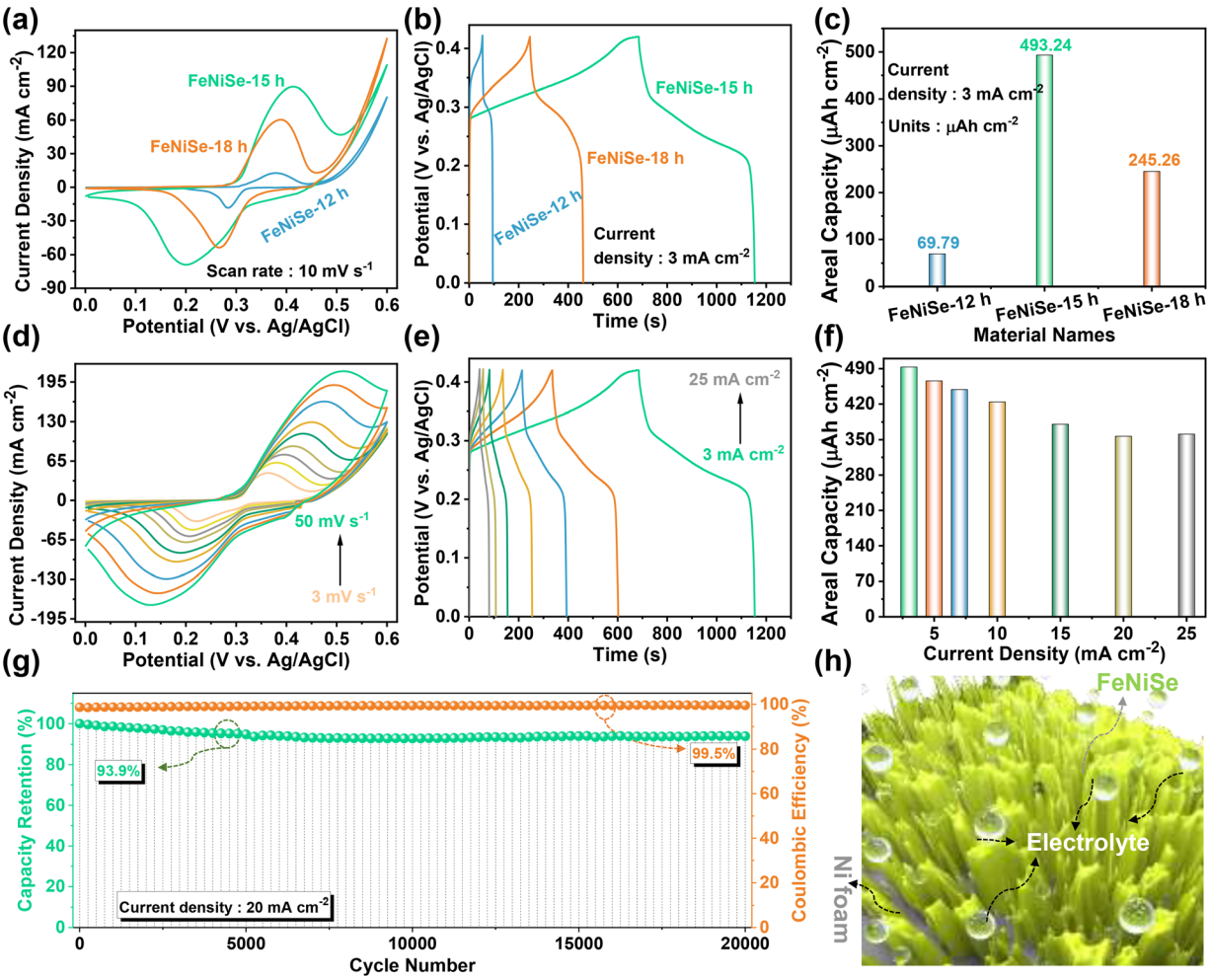

Fig. 3 Comparative (a) CV curves, (b) GCD curves, and (c) areal capacity values of the prepared FeNiSe-12 h, FeNiSe-15 h, and FeNiSe-18 h electrodes. (d) CV curves, (e) GCD curves, and (f) areal capacity values of the FeNiSe-15 h electrode. (g) Cycling stability test performed at 20 mA cm^{-2} and (h) schematic diagram of the morphological merits of the FeNiSe-15 h electrode.

redox reactions and inter-valence charge transfer between Fe^{2+}/Fe^{3+} and Ni^{2+}/Ni^{3+} pairs, demonstrating the typical battery-type nature of the electrodes. The oxidation and reduction reactions can be given by the equations below:[49–52]

$$2FeNiSe + 4OH^- \leftrightarrow 2FeSeOH + 2NiSeOH + e^- \quad (1)$$

$$FeSeOH + OH^- \leftrightarrow FeSeO + H_2O + e^- \quad (2)$$

$$NiSeOH + OH^- \leftrightarrow NiSeO + H_2O + e^- \quad (3)$$

The FeNiSe-15 h electrode has a larger CV area than the other prepared electrodes, resulting in better charge storage capability, which may be attributed to the complementary features and adequate synergism of Fe and Ni ions. In addition, the designed electrodes were further investigated by galvanostatic charge–discharge (GCD) analysis at 3 mA cm^{-2}, as presented in Fig. 3(b). This result is very consistent with the CV result. The obtained results suggest that the CV and GCD shapes show obvious potential platforms related to the battery-type behavior of the active components and their reliable faradaic redox properties. Moreover, compared to the other electrodes, the FeNiSe-15 h electrode has a particularly long discharge time, demonstrating that it can endure large charges and provide a greater capacity/capacitance. Besides, at the same current density, the areal capacity of the prepared electrodes was estimated (eqn (S1)†) using the discharge time from the GCD profiles. From Fig. 3(c), the FeNiSe-15 h electrode delivered a higher areal capacity (493.2 μA h cm^{-2}) than the FeNiSe-12 h (69.7 μA h cm^{-2}) and FeNiSe-18 h (245.2 μA h cm^{-2}) electrodes. Also, the FeNiSe-15 h electrode exhibited better performance than those of previously published selenide-based reports, as presented in Table 1. To evaluate the electrochemical characteristics of the FeNiSe-15 h electrode, the CV and GCD measurements were performed on comparable electrodes such as FeNiSe-12 h and FeNiSe-18 h. The CV curves of the FeNiSe electrodes at various scan rates from 3 to 50 mV s^{-1} within an applied potential from 0 to 0.6 V *vs.* Ag/AgCl are presented in Fig. 3(d) and Fig. S1(a) and (d).† All of the CV curves appear to have substantial redox features associated with the exceptional faradaic nature of the Fe^{2+}/Fe^{3+} and Ni^{2+}/Ni^{3+} active portions. The slopes of the CV curves remained stable, while the currents at the oxidation and reduction peaks increased progressively as the scan rate increased, showing quick redox processes at a comparatively low internal resistance.[44] During the CV test, the CV curves shifted slightly towards the higher potential side in the oxidation medium, while in reduction, the peaks shifted towards the lower potential side. The variation in potential is due to the oxidation and reduction peaks increasing as a result of internal resistance and the influence of polarization.[53] Also, the GCD measurements at different current densities from 3 to 25 mA cm^{-2} in the potential window of 0–0.42 V *vs.* Ag/AgCl are shown in Fig. 3(e) and Fig. S1(b) and (e).† The almost symmetric GCD curves represent quick redox reaction kinetics as well as improved reversibility. Fascinatingly, the FeNiSe-15 h electrode revealed longer discharge times than the other electrodes. The non-linear curves with evident potential plateaus indicate that the electrode shows a battery-like performance, which is consistent with the CV data. The areal capacities of all the electrodes were estimated depending on the GCD discharge times, as presented in Fig. 3(f) and Fig. S1(c) and (f).† The battery-like nature of FeNiSe-15 h led to enhanced electrochemical reactions with larger areal capacities of 493.2, 465.7, 448.6, 424.1, 380.6, 356.8, and 351 μA h cm^{-2} at different current densities of 3, 5, 7, 10, 15, 20, and 25 mA cm^{-2}, respectively. Since faradaic processes occur mostly at the outer surfaces of active electrode materials, the usage rate of active electrode material gradually decreases with an increase in the current density,

Table 1 Comparative electrochemical properties of previously published selenide-based electroactive materials with FeNiSe/Ni foam electrode

Electrode material	Method	Electrolyte	Test condition	Capacitance/Capacity	Ref.
$FeSe_2$	Solvothermal	1 M KOH	1 A g^{-1}	362.1 F g^{-1}	21
$Co_{0.85}Se$	Solvothermal	2 M KOH	0.5 A g^{-1}	294 F g^{-1}	62
NiSe	Solvothermal	2 M KOH	1 A g^{-1}	54.2 mA h g^{-1}	63
$NiSe_2$	Hydrothermal	1 M KOH	1 A g^{-1}	8.3 mA h g^{-1}	64
$CoSe_2$	Microwave	6 M KOH	1 A g^{-1}	333 F g^{-1}	65
SnSe	Reflux	6 M KOH	0.5 A g^{-1}	34.8 mA h g^{-1}	66
CoSe	Hydrothermal	2 M KOH	1 A g^{-1}	70.6 mA h g^{-1}	67
$NiSe_2$	Solvothermal	1 M KOH	3 A g^{-1}	466 F g^{-1}	68
$NiCo_2Se_4$	Hydrothermal	6 M KOH	1 A g^{-1}	461 F g^{-1}	69
$GeSe_2$	Thermal evaporation	1 M KOH	1 A g^{-1}	300.1 F g^{-1}	70
CoSe/C	Annealing	2 M KOH	1 A g^{-1}	658 F g^{-1}	71
$NiCoSe_2$	Annealing	2 M KOH	1 A g^{-1}	300.2 F g^{-1}	72
$(Ni,Co)Se_2$	Solvothermal	2 M KOH	1 A g^{-1}	106 mA h g^{-1}	73
Co_3Se_4/N-CNT	Solvothermal	2 M KOH	2 mV S^{-1}	114 F g^{-1}	74
$NiCu(OH)_2$@Ni–Cu–Se	Electrodeposition	1 M KOH	1 A g^{-1}	264.91 F g^{-1}	75
La_2Se_3	SILAR	0.8 M $LiClO_4$	0.5 mA cm^{-2}	170 F g^{-1}	76
Se-NFHC	Hydrothermal	—	1 A g^{-1}	744 F g^{-1}	77
$NiCuSe_2$	Electrodeposition	1 M KOHs	0.25 mA cm^{-2}	17.36 mA h g^{-1}	78
$Fe_3Se_4/Ni_{0.85}Se$	Solvothermal	2 M KOH	3 mA cm^{-2}	493.2 μA h cm^{-2} 113.9 mA g^{-1} 784.4 F g^{-1}	This work

and thus the total capacity of the electrode decreases. The battery-like FeNiSe-15 h electrode demonstrated an improved capacity retention of about 71.1%, even at a higher current density of 25 mA cm^{-2}. The FeNiSe-15 h electrode delivered high areal capacity and good rate capability due to its hierarchical design, good surface area, and quick ion transport kinetics. Additionally, the long-lasting cycling ability of the FeNiSe-15 h electrode was tested by continuous charging and discharging for 20 000 cycles at 20 mA cm^{-2} with an excellent capacity retention of 93.9%, while the coulombic efficiency was calculated to be 99.5% (Fig. 3(g)). In Fig. S3,† the FeNiSe-12 h (92.3%) and FeNiSe-18 h (98.2%) electrodes also exhibited good cycling stability. Such excellent electrochemical performance of the battery-like FeNiSe-15 h electrode is mainly ascribed to the following features, as shown in Fig. 3(h). (1) The combination of Fe and Ni ions enhances the redox properties. (2) Directly developed active material on the 3D conductive current collector together with the *in situ* selenization processes can effectively increase the electrical conductivity and charge transfer kinetics by circumventing the usage of conductive binders and additives.[54,55] (3) The synergetic contacts between the active FeNiSe-15 h SLA material and Ni foam support strengthen mechanical and physical stability during the cycling test.

To investigate the possible applicability of FeNiSe heterostructures in charge storage devices, an AHC was constructed in a 2 M KOH aqueous solution by assembling FeNiSe-15 h as a positive electrode and commercial AC-coated Ni foam (AC/Ni foam) as a negative electrode. Depending on eqn (S3),† the mass balance of the negative electrode was estimated to be 7.5 mg cm^{-2}. Fig. 4(a) illustrates the construction of the FeNiSe-15 h//AC device. The electrochemical properties of AC/Ni foam as the negative electrode were also measured in a three-electrode set-up using 2 M KOH electrolyte. The CV and GCD tests within a potential range from −1 to 0 V *vs.* Ag/AgCl at different sweep rates and current densities are presented in Fig. S5.† From these figures, the CV and GCD curves of the AC/Ni foam electrode revealed symmetrical behavior at higher scan rates and current densities, suggesting good reversibility. To verify the suitable working voltage window, the fabricated AHC device was measured at different voltages from 1.2 to 1.6 V at a fixed scan rate, as shown in Fig. 4(b). Similarly, the GCD test was also carried out at a constant current density of 15 mA cm^{-2}, as presented in Fig. 4(c). With an operational voltage window smaller than 1.2 V, the CV curves with a nearly rectangular shape were achieved. When the voltage approached 1.5 V, partial oxidization and reduction peaks were detected, indicating incomplete surface faradaic redox reactions of the electrode materials due to inadequate kinetics. Once the voltage approached 1.6 V, well-developed oxidization and reduction peaks existed, suggesting that the created device shows complete faradaic redox processes with improved reversibility. Beyond the applied potential window of 1.6 V, the CV curve was polarized, providing clear evidence for the OER in the positive material. Furthermore, the CV curve was tested at the same scan rate with an applied voltage of 1.8 V, which shows a slight hump after reaching 1.6 V in the positive region, as presented in Fig. S6(a).† This unfavorable hump is due to oxygen/hydrogen evolution processes that occur after 1.6 V. When the operating potential window of the device exceeds its ideal value, these processes cause the lifetime of the devices to decline drastically by degrading the electrode materials. In addition, the GCD analysis was carried out at 15 mA cm^{-2} in the same voltage window of 0–1.8 V, as shown in Fig. S6(b).† The charge profile of the AHC device became saturated after reaching 1.6 V, implying the saturated charge storage capacity capability of FeNiSe-15 h active sites. As a result, we selected a working voltage window of 0–1.6 V for the AHC device. Within this working voltage window, the electrochemical characteristics of the AHC were explored further. Fig. 4(d) shows the CV curves of the AHC at various scan rates with an applied voltage window of 1.6 V. It is evident that the charge transport and ion diffusion mechanisms affect the capacitive performance of the AHC. The apparent redox peaks, along with a low peak potential displacement, imply that the device exhibits battery-like functionality. The integral area encompassed by the CV curve steadily increases with sweep rate, indicating improved rate performance and reversible redox processes. Moreover, the non-linear charge–discharge profiles were tested at various current densities from 3 to 50 mA cm^{-2} (Fig. 4(e)). The charge storage properties of the assembled AHC device agree well with the redox activity. The areal capacity as a function of the current density of the fabricated AHC is shown in Fig. 4(f). The AHC exhibited a high areal capacity of 453 μA h cm^{-2} at a current density of 3 mA cm^{-2}. In addition, to study the rate capability of the AHC, the electrochemical properties were measured at various current densities from 3 to 50 mA cm^{-2} within the applied voltage (Fig. 4(g)). The obtained areal capacities were about 454, 438.6, 419.2, 407, 380.7, 344.3, 334.1, 319.4, 290.7, and 269.7 μA h cm^{-2} at current densities of 3, 5, 7, 10, 15, 20, 25, 30, 40, and 50 mA cm^{-2}, respectively. After the current density had been ramped up, when the current density returned to 3 mA cm^{-2}, the obtained areal capacity was ~454 μA h cm^{-2}. At the end of 10 cycles, the areal capacity obtained was ~453.5 μA h cm^{-2}. Even at 50 mA cm^{-2}, the AHC showed a good areal capacity of 269.7 μA h cm^{-2}. As a result, the AHC demonstrated a rate capability of 59.4% even at a higher current value of 50 mA cm^{-2}. Energy and power densities are two key parameters for estimating the energy storage properties in an AHC. Using eqn (S4) and (S5),†[56] the energy and power density values were estimated and the related Ragone plot is presented in Fig. 4(h). The as-assembled AHC exhibited an energy density value of ~0.36 mWh cm^{-2} and a power density value of 56.6 mW cm^{-2}. Such energy storage performance is higher than those of the previously reported selenide or sulfide hybrid/asymmetric devices in Table S1.† The cycling performance and coulombic efficiency profiles of the AHC for 25 000 continuous charging–discharging cycles performed at 40 mA cm^{-2} are shown in Fig. 4(i). Interestingly, the AHC retained 82.2% of its primary cycle capacity after the long-term cycling process, while the coulombic efficiency was estimated to be 99%. Electrochemical impedance spectroscopy (EIS) plots were

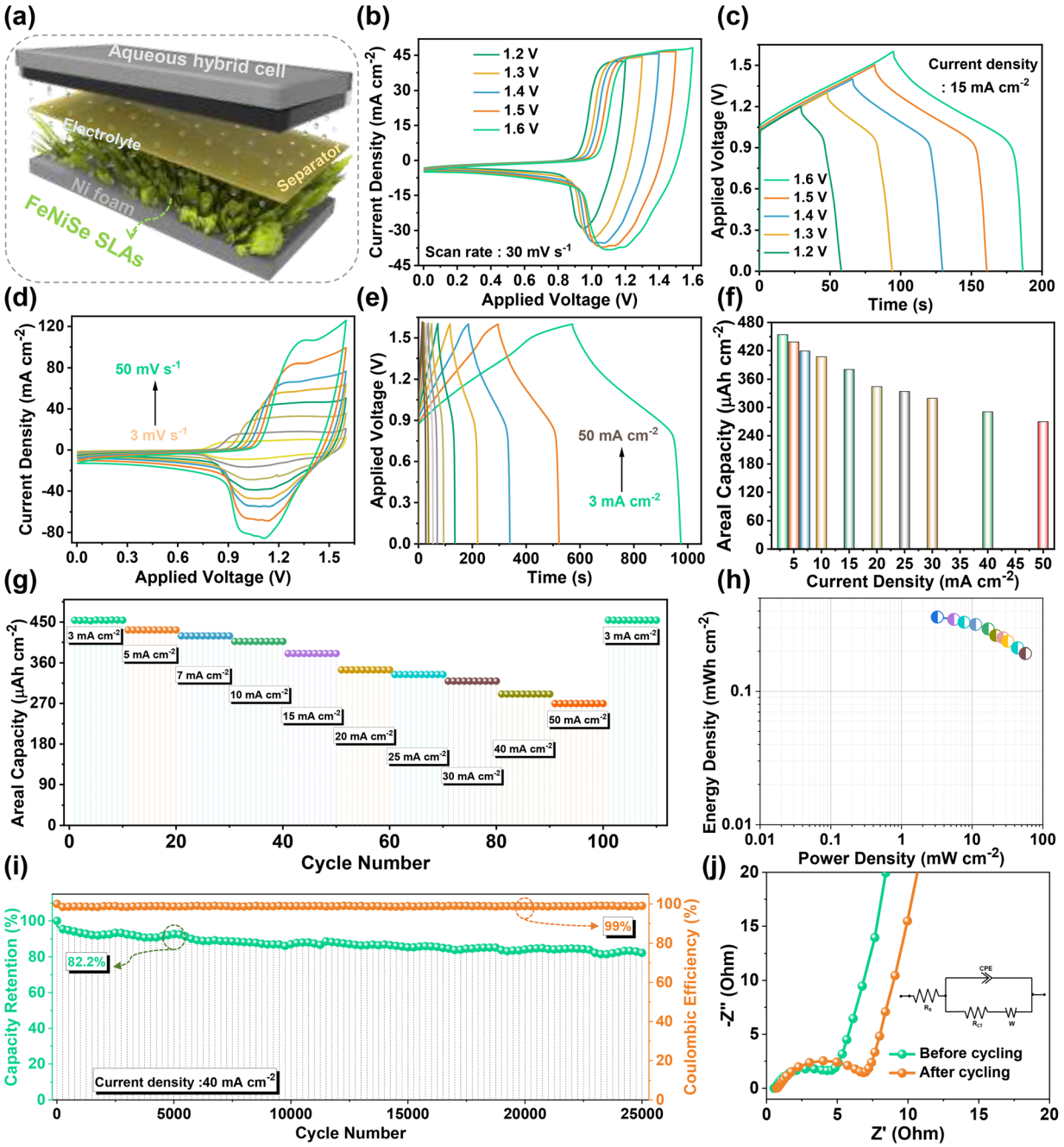

Fig. 4 (a) Schematic diagram of the AHC fabricated with FeNiSe-15 and AC as the positive and negative electrodes, respectively. (b) CV and (c) GCD profiles for the device were measured at different voltages at constant scan rates and current densities, respectively. (d) CV curves, (e) GCD curves, (f) areal capacity values, and (g) rate performance at different current densities. (h) Ragone plot, (i) cycling stability tested at 40 mA cm^{-2}, and (j) EIS plots before and after the cycling test of the device.

measured to study the internal resistance of the fabricated AHC. Fig. 4(j) shows the Nyquist plots before and after the cycling test for the AHC. From this figure, the Nyquist plots consist of two main parts. Both plots comprise a semicircle and a slanted line, suggesting low solution resistance (R_s) and charge transfer resistance (R_{ct}) values owing to the better diffusion rate of ions into the bulk electrode material. Comparatively, before the cycling test, the R_s value was slightly altered with a further increase from 0.54 to 0.72 Ω, and the R_{ct} value increased from 4.1 to 6.29 Ω. The small alteration in the slanted line in the low-frequency region reveals the good ion diffusion ability and improved electrochemical performance of the fabricated electrodes.[57] By considering the obtained results, the pouch-like FeNiSe-15 h//AC could effectively enable high-energy storage with a suitable lifespan and elucidate a new path for assembling other positive materials.

Despite its large energy storage capacity, an AHC is essentially exposed for employment in practical applications. As a result, we investigated the real-life applicability of the AHC for powering up various electronic appliances. The working voltage was extended to 3.2 V by joining two AHCs in series to function in a variety of electronic applications, as presented in Fig. 5(a). Moreover, eco-friendly features and cost-effectiveness are important in sustainable energy policy. Wind energy, as we know, is a green and plentiful power source. Harvesting wind electricity might certainly solve all of humanity's energy issues and diminish the dependence on fossil fuel consumption for day-to-day energy needs. However, a decrease in light intensity as a result of climatic changes results in fluctuations and discontinuous generation of electric sources. As a result, there is an urgent need to employ effective energy storage devices capable of storing wind energy determinedly over a short period of time. To overcome the constraint of wind discontinuity, we attempted to store wind energy in an energy storage device. A commercially available portable wind turbine was used to charge the AHC devices connected in series before and after charging, as shown in Fig. S7.† Fig. 5(b) demonstrates the corresponding self-powered charging wind turbine station. Moreover, the as-stored energy was employed to power up the cap lights on a night-cap light-emitting diode (LED) headlamp, as shown in Fig. 5(c). From this figure, five white LEDs were illuminated for up to 15 min, as presented in Fig. 5(c-(i–iii)), before and after connection to the AHCs. Likewise, an LED crystal key flashlight was also driven by charging the wind energy storing AHCs, which was powered up for ~10 min. Fig. 5(d-(i–iii)) show photographic images of the LED crystal key flashlight before and after connection to the AHCs. As a proof of concept, this self-powered unit demonstrates that the fabricated high-performance AHC with FeNiSe SLAs has considerable potential for future portable electronic appliances and energy storage systems.

On the other hand, energy creation has also become necessary in recent times with the exhaustion of typical non-renewable resources and the ever-increasing problems of global warming. Hence, the capability of FeNiSe materials as catalysts to manipulate OER performance was also studied in an alkaline KOH electrolyte solution. A linear sweep voltammetry (LSV) test was performed on the FeNiSe-12 h, FeNiSe-15 h, and FeNiSe-18 h catalysts at a low scan rate of 2 mV s^{-1} in a conventional three-terminal system using 2 M KOH electrolyte. Fig. 6(a) shows the resulting LSV profiles of the FeNiSe-12 h, FeNiSe-15 h, and FeNiSe-18 h catalysts. The potential values were converted into the reversible hydrogen electrode (RHE) format. Among them, the FeNiSe-15 h catalyst unveiled an OER process at a lower potential that requires its high catalytic activity. Also, it disclosed maximum catalytic capability com-

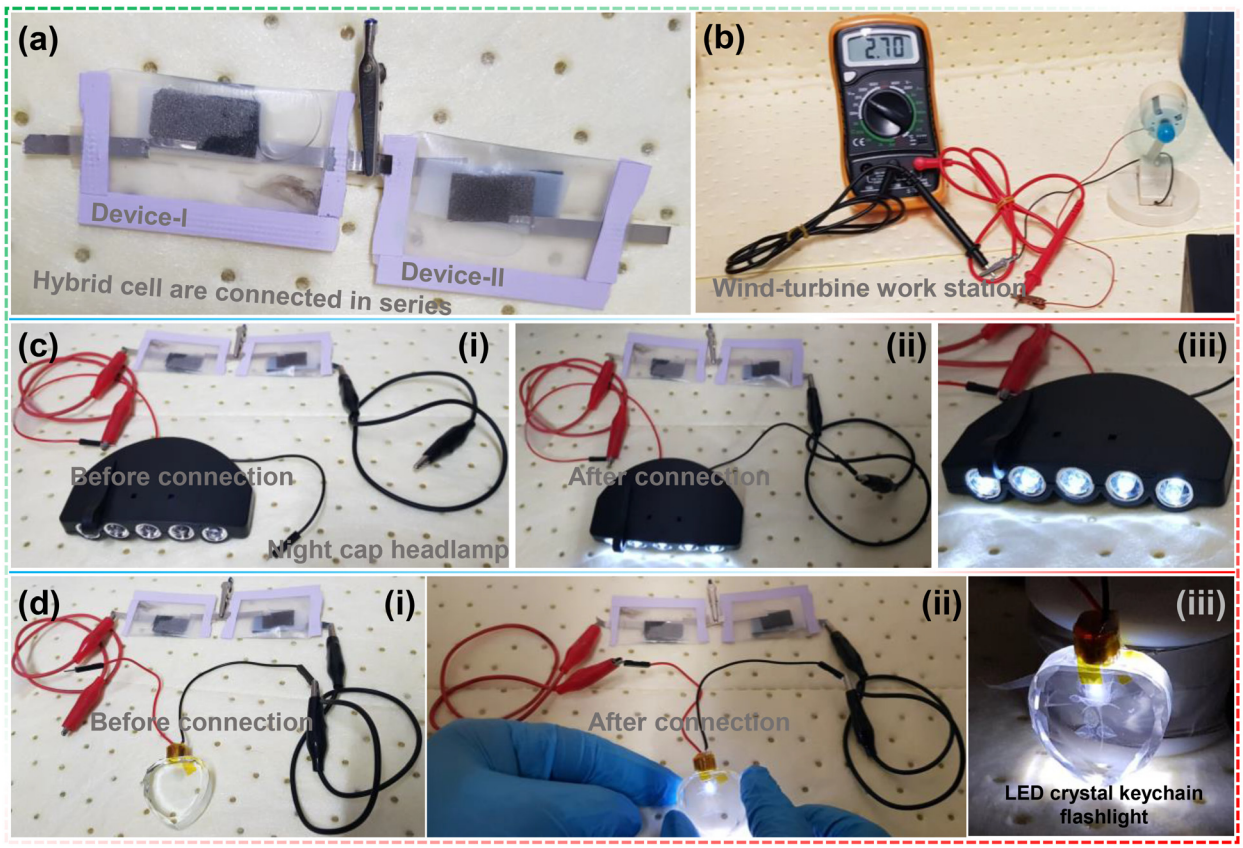

Fig. 5 Photographic images of practical applications: (a) two AHCs connected in series to extend the potential, packaged with transparent parafilm. (b) Wind energy conversion to charge the designed AHCs. (c) Cap lights on night-cap LED headlamp before and after connection. (d) LED crystal key flashlight before and after connection to the AHCs.

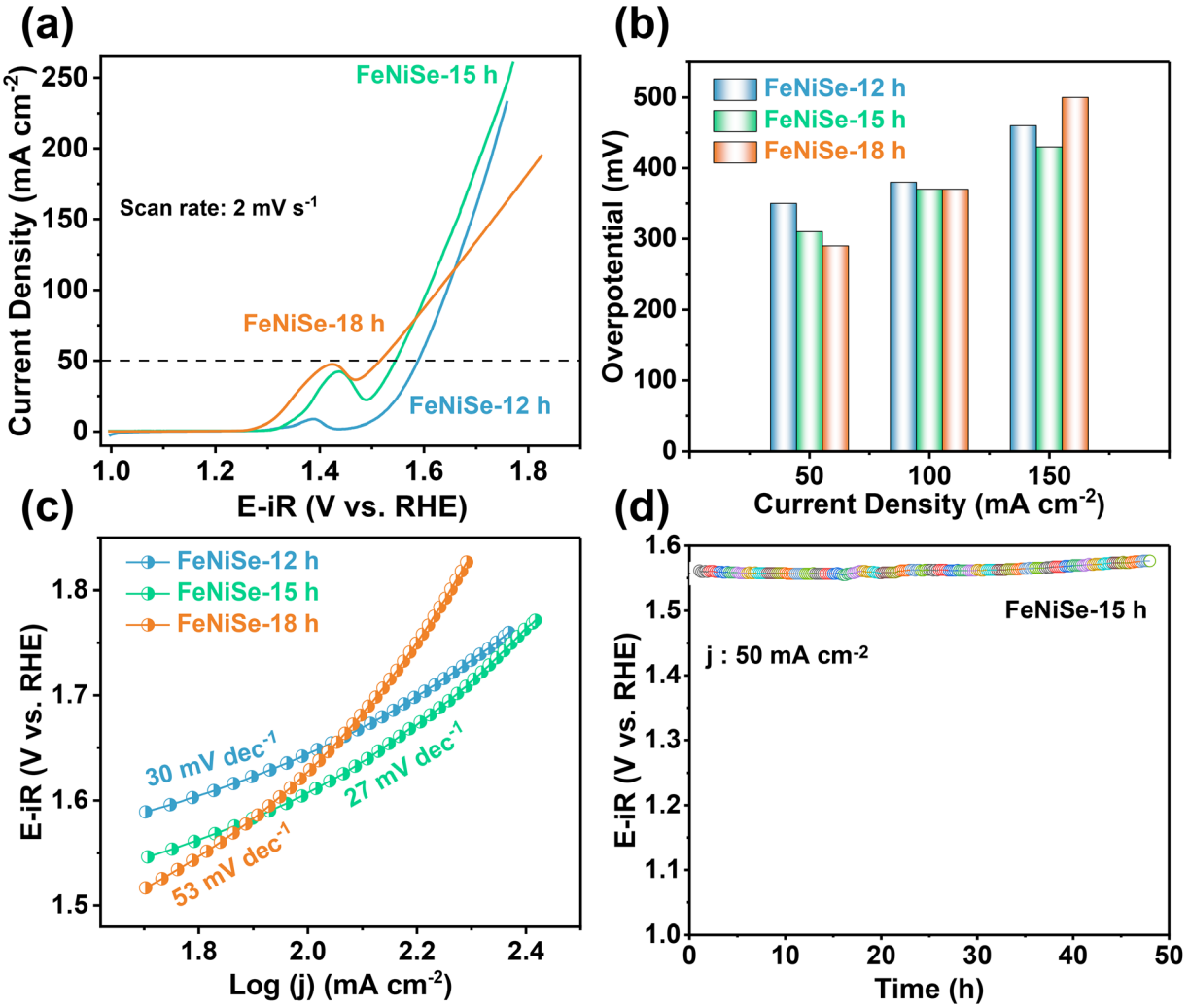

Fig. 6 (a) LSV curves, (b) overpotential values, and (c) Tafel diagram of FeNiSe-12 h, FeNiSe-15 h, and FeNiSe-18 h catalysts. (d) Durability test profile of the FeNiSe-15 h catalyst.

pared to the FeNiSe-12 h and FeNiSe-18 h catalysts in attaining a current density of 50 mA cm^{-2}. Moreover, the FeNiSe-15 h catalyst continues the same tendency in the achievement of 150 and even 100 mA cm^{-2} current densities, whereas the FeNiSe-12 h and FeNiSe-18 h catalysts lag behind the FeNiSe-15 h catalyst in accomplishing all these current densities. Fig. 6(b) shows a bar diagram of the overpotential (OP) values of all the catalysts at various current densities. The FeNiSe-15 h catalyst required OP values of only 310, 370, and 430 mV to drive the current densities of 50, 100, and 150 mA cm^{-2}, respectively. However, the FeNiSe-18 h catalyst exhibited slightly higher OP values of 290, 378, and 500 mV, and the FeNiSe-12 h catalyst showed even higher OP values of 350, 380, and 460 mV to reach the same current densities, respectively. The Tafel slopes of all the FeNiSe catalysts are plotted in Fig. 6(c). It can be observed that the FeNiSe-15 h catalyst exhibited a lower Tafel slope of 27 mV dec^{-1} than those of the FeNiSe-12 h (30 mV dec^{-1}) and FeNiSe-18 h (53 mV dec^{-1}) catalysts. Furthermore, the longevity of the FeNiSe-15 h catalyst was investigated by the chronopotentiometry (CP) method at a constant current density of 50 mA cm^{-2}, and the properties attained are presented in Fig. 6(d). Interestingly, the FeNiSe-15 h catalyst exhibited almost steady electrocatalytic activity for 48 h of the longevity test. The good OER performance of the FeNiSe-based catalysts can be explained as follows: from the FE-SEM images of FeNiSe-12 h, it can be seen that slight roughness on the Ni foam occurs when the growth of SLAs begins, which signifies that the reaction time of 12 h may not be enough to grow the SLAs completely. Due to these specific undeveloped SLAs, the FeNiSe-12 h catalyst has relatively small fractions of active regions. Consequently, the effectiveness of the catalyst in facilitating OER is reduced, leading to lower performance overall. After extending the reaction time to 15 h, noticeable improvements in the SLAs of the corresponding catalyst, FeNiSe-15 h, were observed. Compared to the FeNiSe-12 h catalyst, the FeNiSe-15 h catalyst exhibited well-developed SLAs with better lateral dimensions. Consequently, the FeNiSe-15 h catalyst demonstrated the enhanced performance due to

its ability to accommodate a larger number of electrolyte ions within its well-developed SLAs, leading to improved and efficient OER activity. Additionally, the FeNiSe-15 h catalyst exhibited a higher active mass of deposited material, of 4.33 mg cm^{-2}, compared to the FeNiSe-12 h catalyst (2.58 mg cm^{-2}), which resulted in improved catalytic performance for the FeNiSe-15 h catalyst. However, when the growth time was further extended to 18 h, the SLAs experienced shrinkage, and the formation of lumps became evident. Thus, the availability of active sites decreased, and the diffusion of electrolytes became sluggish. Furthermore, the excessive assembly of SLAs might result in poor adherence to the Ni foam. As a result, the FeNiSe-18 h catalyst, with a mass of approximately 3.85 mg cm^{-2}, exhibited lower OER activity compared to the FeNiSe-15 h catalyst but still higher than that of the FeNiSe-12 h catalyst. Moreover, to investigate the ion–electron transport kinetics as well as the resistive features, electrochemical impedance spectroscopy (EIS) analysis was performed for the FeNiSe-based catalysts. Fig. S2† shows the EIS plots of the FeNiSE-12 h, FeNiSe-15 h, and FeNiSe-18 h catalysts tested in the frequency range between 100 kHz and 0.01 Hz within the applied open circuit potential. The EIS plots of all the FeNiSe-based catalysts contain a low semicircle arc in the higher frequency region and a slanted line in the lower frequency region. In the higher frequency region, the intercept value on the '*Z*' real of the FeNiSe-15 h catalyst exhibited smaller internal resistance and electrolyte resistance (R_s) compared to the FeNiSe-12 h and FeNiSe-18 h catalysts. Compared with the FeNiSe-15 h catalyst, the EIS plot of the other catalysts showed higher charge transfer resistance (R_{ct}), which specifies that the electrons and OH^- could be transferred efficiently at the interface between the electrolyte and active material. Furthermore, the EIS tests suggest that the FeNiSe-15 h catalyst shows higher catalytic performance than the other prepared catalysts. The R_s and R_{ct} values were obtained with slight variations, indicating the good electrical conductivity of all the prepared catalysts. The R_s and R_{ct} values of FeNiSe-12 h, FeNiSe-15 h, and FeNiSe-18 h were estimated to be 0.55, 0.31, and 0.53 Ω and 0.19, 0.09, and 0.12 Ω, respectively. Moreover, the electrochemical surface area (C_{dl} or ECSA) of the fabricated catalysts was estimated, which is one of the most elementary and important characteristics of catalyst–electrolyte interfaces. It is the area of the catalyst that is available to the electrolyte for interaction (charge storage and/or transfer) and plays a crucial role in the catalytic process.[58] Higher C_{dl} or ECSA implies better accessibility of electrolyte ions to more electroactive sites, resulting in improved electrochemical performance.[58] The C_{dl} or ECSA values of the FeNiSe-based catalysts were calculated from the double-layer capacitance (DLC), and they can be obtained from the non-redox region of the CV (Fig. S4(a–c)†) plots of the catalyst within a potential window of 0 to 0.1 V in 2 M KOH solution. The ECSA can be estimated with the following equation:[59,60]

$$\mathrm{ECSA} = C_{dl}/C_s,$$

where C_{dl} is the DLC, which can be obtained from the slope of scan rate *vs.* current density plots (based on the CV data, Fig. S4(d)†). C_s is the standard specific electrochemical DLC, and its value is taken as 40 μF cm^{-2} for KOH electrolyte.[61] For the estimation of C_{dl} or ECSA of the FeNiSe-based catalysts *via* the DLC method, the respective CV curves were recorded in 2 M KOH electrolyte within a potential range of 0.1 V at scan rates between 30 and 100 mV s^{-1} to obtain the double-layer region. From the slope of scan rate *vs.* current density plots, The C_{dl} value was obtained as 0.91, 1.58, and 1.48 mF for FeNiSe-12 h, FeNiSe-15 h, and FeNiSe-18 h catalysts, respectively. Finally, for the FeNiSe-12 h, FeNiSe-15 h, and FeNiSe-18 h catalysts, the calculated ECSA values were 22.7, 39.5, and 37 cm^2, respectively.

4. Conclusions

In summary, we prepared binary FeNiSe heterostructures on Ni foam as a favorable electroactive material *via* a facile one-pot solvothermal technique for electrochemical energy storage devices. The deposited FeNiSe active material, with proper contact with the underlying current collector, sustains a large interface for the penetration of electrons/ions and facilitates an improvement in electrochemical reactions. At 3 mA cm^{-2}, the as-prepared FeNiSe-15 h electrode demonstrated a high areal capacity of 493.2 μA h cm^{-2}, which is comparatively higher than that of the other electrodes with a high rate capability of 71.1% even at a high current density of 25 mA cm^{-2}. Moreover, the FeNiSe-15 h electrode exhibited excellent cycling retention of 93.9% even after 20 000 continuous GCD cycles. Also, in OER tests, the same FeNiSe-15 h catalyst produced superior catalytic activity to the FeNiSe-12 h or FeNiSe-18 h catalysts. In particular, the FeNiSe-15 h catalyst showed the specific requirement of reaching only a low overpotential (310 mV) to achieve 50 mA cm^{-2} of current density, and in addition, it displayed a lower Tafel slope (27 mV dec^{-1}) than those of the FeNiSe-12 h and FeNiSe-18 h catalysts. Furthermore, the FeNiSe-15 h catalyst showed good stability without much enhancement in the required voltage. The constructed AHC exhibited high energy (0.36 mW h cm^{-2}) and power (56.6 mW cm^{-2}) densities with a good rate capability of 59.4% even at the higher current density of 50 mA cm^{-2}. In addition, the as-fabricated device demonstrated excellent cycling retention of 82.2% even after 25 000 charge–discharge cycles. Furthermore, two AHCs were effectively joined into a unit self-powered by a wind turbine to power up various electronic devices for a long time, which further validates the potency of the assembled AHC for real-time applicability.

Conflicts of interest

The authors declare no conflict of interest.

Acknowledgements

This work was supported by the National Research Foundation of Korea (NRF) grant funded by the Korean government (MSIP) (No. 2018R1A6A1A0302570).

References

1 S. Zhang and N. Pan, *Adv. Energy Mater.*, 2015, **5**, 1401401.
2 Y. Shao, M. F. El-Kady, J. Sun, Y. Li, Q. Zhang, M. Zhu, H. Wang, B. Dunn and R. B. Kaner, *Chem. Rev.*, 2018, **118**, 9233–9280.
3 P. Simon, Y. Gogotsi and B. Dunn, *Science*, 2014, **343**, 1210–1211.
4 M. Salanne, B. Rotenberg, K. Naoi, K. Kaneko, P. L. Taberna, C. P. Grey, B. Dunn and P. Simon, *Nat. Energy*, 2016, **1**, 16070.
5 Q. Zhu, D. Zhao, M. Cheng, J. Zhou, K. A. Owusu, L. Mai and Y. Yu, *Adv. Energy Mater.*, 2019, **9**, 1901081.
6 F. Wang, X. Wu, X. Yuan, Z. Liu, Y. Zhang, L. Fu, Y. Zhu, Q. Zhou, Y. Wu and W. Huang, *Chem. Soc. Rev.*, 2017, **46**, 6816–6854.
7 A. Muzaffar, M. B. Ahamed, K. Deshmukh and J. Thirumalai, *Renewable Sustainable Energy Rev.*, 2019, **101**, 123–145.
8 D. Yu, Q. Qian, L. Wei, W. Jiang, K. Goh, J. Wei, J. Zhang and Y. Chen, *Chem. Soc. Rev.*, 2015, **44**, 647–662.
9 X. Ye, J. Fan, Y. Min, P. Shi and Q. Xu, *Nanoscale*, 2021, **13**, 14854–14865.
10 J.-S. Lee, J. W. An, S. Bae and S.-K. Lee, *Appl. Sci. Converg. Technol.*, 2022, **31**, 79–84.
11 K. Chang, D. T. Tran, J. Wang, N. H. Kim and J. H. Lee, *J. Mater. Chem. A*, 2022, **10**, 3102–3111.
12 R. Qin, P. Wang, Z. Li, J. Zhu, F. Cao, H. Xu, Q. Ma, J. Zhang, J. Yu and S. Mu, *Small*, 2022, **18**, 2105305.
13 H.-L. Li, Y.-Y. Wang, C.-M. Liu, S.-M. Zhang, H.-F. Zhang and Z.-W. Zhu, *Int. J. Hydrogen Energy*, 2022, **47**, 20718–20728.
14 P. M. Bodhankar, P. B. Sarawade, G. Singh, A. Vinu and D. S. Dhawale, *J. Mater. Chem. A*, 2021, **9**, 3180–3208.
15 G. Liu, C. Shuai, Z. Mo, R. Guo, N. Liu, Q. Dong, J. Wang, H. Pei, W. Liu and X. Guo, *Electrochim. Acta*, 2021, **385**, 138452.
16 X. Xu, Y. Liu, X. Luo, G. Ma, F. Tian, Y. Li, D. Zhang and J. Yang, *Energy Storage Mater.*, 2021, **40**, 189–196.
17 Y. Sun, K. Mao, Q. Shen, L. Zhao, C. Shi, X. Li, Y. Gao, C. Li, K. Xu and Y. Xie, *Adv. Funct. Mater.*, 2022, **32**, 2109792.
18 A. K. Das, B. Ramulu, E. G. Shankar and J. S. Yu, *Chem. Eng. J.*, 2022, **429**, 132486.
19 B. K. Deka, A. Hazarika, S. Lee, D. Y. Kim, Y.-B. Park and H. W. Park, *Nano Energy*, 2020, **73**, 104754.
20 M. Li, X. Zheng, L. Xie, Y. Yu and J. Jiang, *New J. Chem.*, 2021, **45**, 14808–14814.
21 P. Santhoshkumar, G. Nagaraju, N. Shaji, G. S. Sim, M. Nanthagopal, S. C. Sekhar, J. S. Yu and C. W. Lee, *Electrochim. Acta*, 2020, **356**, 136833.
22 R. Balaji, J. Balamurugan, T. T. Nguyen, N. H. Kim and J. H. Lee, *Chem. Eng. J.*, 2020, **390**, 124557.
23 R. Hou, G. S. Gund, K. Qi, P. Nakhanivej, H. Liu, F. Li, B. Y. Xia and H. S. Park, *Energy Storage Mater.*, 2019, **19**, 212–241.
24 B. Liu, Y.-F. Zhao, H.-Q. Peng, Z.-Y. Zhang, C.-K. Sit, M.-F. Yuen, T.-R. Zhang, C.-S. Lee and W.-J. Zhang, *Adv. Mater.*, 2017, **29**, 1606521.
25 J. Wang, Y. Zhu, S. Li, S. Zhai, N. Fu, Y. Niu, S. Hou, J. Luo, S. Mu and Y. Huang, *Chem. Commun.*, 2022, **58**, 8846–8849.
26 B. Ye, X. Cao, Q. Zhao and J. Wang, *Ind. Eng. Chem. Res.*, 2020, **59**, 14163–14171.
27 S. Song, L. Yu, X. Xiao, Z. Qin, W. Zhang, D. Wang, J. Bao, H. Zhou, Q. Zhang, S. Chen and Z. Ren, *Mater. Today Phys.*, 2020, **13**, 100216.
28 S. Kim and H. Yoo, *ACS Sustainable Chem. Eng.*, 2020, **8**, 13859–13867.
29 Z. Wang, J. Li, X. Tian, X. Wang, Y. Yu, K. A. Owusu, L. He and L. Mai, *ACS Appl. Mater. Interfaces*, 2016, **8**, 19386–19392.
30 Y. Guo, C. Zhang, J. Zhang, K. Dastafkan, K. Wang, C. Zhao and Z. Shi, *ACS Sustainable Chem. Eng.*, 2021, **9**, 2047–2056.
31 D. Zhu, Q. Zhen, J. Xin, H. Ma, H. Pang, L. Tan and X. Wang, *J. Colloid Interface Sci.*, 2021, **598**, 181–192.
32 T. Moon, B. Das, H. Joo and K.-D. Park, *Appl. Sci. Converg. Technol.*, 2023, **32**, 45–47.
33 Y. Huang, L.-W. Jiang, B.-Y. Shi, K. M. Ryan and J.-J. Wang, *Adv. Sci.*, 2021, **8**, 2101775.
34 K. Zhu, X. Zhu and W. Yang, *Angew. Chem., Int. Ed.*, 2019, **58**, 1252–1265.
35 C. Tang, H.-F. Wang, H.-S. Wang, F. Wei and Q. Zhang, *J. Mater. Chem. A*, 2016, **4**, 3210–3216.
36 S. Lee, L. Bai and X. Hu, *Angew. Chem., Int. Ed.*, 2020, **59**, 8072–8077.
37 J. Y. C. Chen, L. Dang, H. Liang, W. Bi, J. B. Gerken, S. Jin, E. E. Alp and S. S. Stahl, *J. Am. Chem. Soc.*, 2015, **137**, 15090–15093.
38 T. Ouyang, Q. Liu, M. Chen, C. Tang, J. Li, C. Zhang, C. He, H. Bao, J. Zhong and M. Hu, *ES Energy Environ.*, 2018, **3**, 88–95.
39 C. Miao, Y. Fang, K. Zhu, C. Zhou, K. Ye, J. Yan, D. Cao, G. Wang, P. Xu and C. Xie, *J. Alloys Compd.*, 2021, **885**, 161004.
40 M. B. Poudel, G. P. Ojha, A. A. kim and H. J. Kim, *J. Energy Storage*, 2022, **47**, 103674.
41 E. Samuel, A. Aldalbahi, M. El-Newehy, H. El-Hamshary and S. S. Yoon, *J. Alloys Compd.*, 2021, **852**, 156929.
42 B. Ramulu, G. Nagaraju, S. C. Sekhar, S. K. Hussain, D. Narsimulu and J. S. Yu, *ACS Appl. Mater. Interfaces*, 2019, **11**, 41245–41257.
43 S. C. Sekhar, G. Nagaraju, B. Ramulu, S. J. Arbaz, D. Narsimulu, S. K. Hussain and J. S. Yu, *Nano Energy*, 2020, **76**, 105016.
44 G. Nagaraju, S. C. Sekhar, B. Ramulu, S. J. Arbaz and J. S. Yu, *Chem. Eng. J.*, 2021, **411**, 128479.
45 X. Xu, G. Fu, Y. Wang, Q. Cao, Y. Xun, C. Li, C. Guan and W. Huang, *Nano Lett.*, 2023, **23**, 629–636.
46 C. Zhu, H. Wang and C. Guan, *Nanoscale Horiz.*, 2020, **5**, 1188–1199.
47 W. Zhao, C. Guo and C. M. Li, *J. Mater. Chem. A*, 2017, **5**, 19195–19202.
48 K. Zhang, M. Park, L. Zhou, G.-H. Lee, W. Li, Y.-M. Kang and J. Chen, *Adv. Funct. Mater.*, 2016, **26**, 6728–6735.

49 C. V. V. Muralee Gopi, A. E. Reddy and H.-J. Kim, *J. Mater. Chem. A*, 2018, **6**, 7439–7448.
50 T. T. Nguyen, J. Balamurugan, V. Aravindan, N. H. Kim and J. H. Lee, *Chem. Mater.*, 2019, **31**, 4490–4504.
51 F. Ma, J. Lu, L. Pu, W. Wang and Y. Dai, *J. Colloid Interface Sci.*, 2020, **563**, 435–446.
52 J. Wang, S. Li, Y. Zhu, S. Zhai, C. Liu, N. Fu, S. Hou, Y. Niu, J. Luo, S. Mu and Y. Huang, *J. Electroanal. Chem.*, 2022, **919**, 116548.
53 D. Khalafallah, M. Zhi and Z. Hong, *Ceram. Int.*, 2021, **47**, 29081–29090.
54 B. K. Deka, A. Hazarika, J. Kim, N. Kim, H. E. Jeong, Y.-B. Park and H. W. Park, *Chem. Eng. J.*, 2019, **355**, 551–559.
55 S. M. Cha, S. C. Sekhar, R. Bhimanaboina and J. S. Yu, *Inorg. Chem.*, 2018, **57**, 8440–8450.
56 G. Nagaraju, S. Tagliaferri, A. Panagiotopoulos, M. Och, R. Quintin-Baxendale and C. Mattevi, *J. Mater. Chem. A*, 2022, **10**, 15665–15676.
57 Y. Yang, J. Zhu, P. Wang, W. Zeng, H. Liu, C. Zhang, Z. Chen, D. Liu, J. Xiao and S. Mu, *J. Alloys Compd.*, 2021, **876**, 160135.
58 A. Roy, A. Ray, S. Saha, M. Ghosh, T. Das, M. Nandi, G. Lal and S. Das, *Int. J. Energy Res.*, 2021, **45**, 16908–16921.
59 Y. Meng, W. Song, H. Huang, Z. Ren, S.-Y. Chen and S. L. Suib, *J. Am. Chem. Soc.*, 2014, **136**, 11452–11464.
60 S. K. Bikkarolla and P. Papakonstantinou, *J. Power Sources*, 2015, **281**, 243–251.
61 A. T. A. Ahmed, H. S. Chavan, Y. Jo, S. Cho, J. Kim, S. Pawar, J. L. Gunjakar, A. I. Inamdar, H. Kim and H. Im, *J. Alloys Compd.*, 2017, **724**, 744–751.
62 H. Peng, G. Ma, K. Sun, Z. Zhang, J. Li, X. Zhou and Z. Lei, *J. Power Sources*, 2015, **297**, 351–358.
63 K. Guo, F. Yang, S. Cui, W. Chen and L. Mi, *RSC Adv.*, 2016, **6**, 46523–46530.
64 N. S. Arul and J. I. Han, *Mater. Lett.*, 2016, **181**, 345–349.
65 S. Liu, S. Sarwar, J. Wang, H. Zhang, T. Li, J. Luo and X. Zhang, *J. Mater. Chem. C*, 2021, **9**, 228–237.
66 C. Zhang, H. Yin, M. Han, Z. Dai, H. Pang, Y. Zheng, Y.-Q. Lan, J. Bao and J. Zhu, *ACS Nano*, 2014, **8**, 3761–3770.
67 Y. Zhu, Z. Huang, Z. Hu, L. Xi, X. Ji and Y. Liu, *Electrochim. Acta*, 2018, **269**, 30–37.
68 A. Chang, C. Zhang, Y. Yu, Y. Yu and B. Zhang, *ACS Appl. Mater. Interfaces*, 2018, **10**, 41861–41865.
69 S. Li, Y. Ruan and Q. Xie, *Electrochim. Acta*, 2020, **356**, 136837.
70 X. Wang, B. Liu, Q. Wang, W. Song, X. Hou, D. Chen, Y.-b. Cheng and G. Shen, *Adv. Mater.*, 2013, **25**, 1479–1486.
71 Y. Zhang, A. Pan, Y. Wang, X. Cao, Z. Zhou, T. Zhu, S. Liang and G. Cao, *Energy Storage Mater.*, 2017, **8**, 28–34.
72 Y. Miao, Y. Sui, D. Zhang, J. Qi, F. Wei, Q. Meng, Y. He, Z. Sun and Y. Ren, *Mater. Lett.*, 2019, **242**, 42–46.
73 H. Lei, J. Zhou, R. Zhao, H. Peng, Y. Xu, F. Wang, H. A. Hamouda, W. Zhang and G. Ma, *Electrochim. Acta*, 2020, **363**, 137206.
74 R. Bose, B. Patil, V. R. Jothi, T.-H. Kim, P. Arunkumar, H. Ahn and S. C. Yi, *J. Ind. Eng. Chem.*, 2018, **65**, 62–71.
75 V. T. Chebrolu, B. Balakrishnan, V. Raman, I. Cho, J.-S. Bak, K. Prabakar and H.-J. Kim, *Appl. Surf. Sci.*, 2020, **506**, 145015.
76 S. J. Patil, V. C. Lokhande, N. R. Chodankar and C. D. Lokhande, *J. Colloid Interface Sci.*, 2016, **469**, 318–324.
77 Y. Meng, S. Lu, H. Lu, Y. Ma, Y. Wu, C. Xie, W. Zhang, M. Qian, G. Li and S. Jin, *Mater. Lett.*, 2021, **304**, 130623.
78 S. K. Shinde, D.-Y. Kim, V. G. Parale, H.-H. Park and H. M. Yadav, *Metals*, 2020, **10**, 1698.